Observation of flat Γ moiré bands in twisted bilayer WSe_2

G. Gatti,[1,*] J. Issing,[1,*] L. Rademaker,[2] F. Margot,[1] T. A. de Jong,[3] S. J. van der Molen,[3] J. Teyssier,[1] T. K. Kim,[4] M. D. Watson,[4] C. Cacho,[4] P. Dudin,[5] J. Avila,[5] K. Cordero Edwards,[1] P. Paruch,[1] N. Ubrig,[1,6] I. Gutiérrez-Lezama,[1,6] A. Morpurgo,[1,6] A. Tamai,[1] and F. Baumberger[1]

[1]*Department of Quantum Matter Physics, University of Geneva, 24 Quai Ernest-Ansermet, 1211 Geneva, Switzerland*
[2]*Department of Theoretical Physics, University of Geneva, 24 Quai Ernest-Ansermet, 1211 Geneva, Switzerland*
[3]*Huygens-Kamerlingh Onnes Laboratory, Leiden Institute of Physics, Leiden University, Leiden, The Netherlands*
[4]*Diamond Light Source, Harwell Campus, Didcot, OX11 0DE, United Kingdom*
[5]*Synchrotron SOLEIL, L'Orme des Merisiers, Saint Aubin-BP 48, 91192 Gif sur Yvette Cedex, France*
[6]*Group of Applied Physics, University of Geneva, 24 Quai Ernest Ansermet, CH-1211 Geneva, Switzerland*

(Dated: November 3, 2022)

The recent observation of correlated phases in transition metal dichalcogenide moiré systems at integer and fractional filling promises new insight into metal-insulator transitions and the unusual states of matter that can emerge near such transitions. Here, we combine real- and momentum-space mapping techniques to study moiré superlattice effects in 57.4° twisted WSe_2 ($tWSe_2$). Our data reveal a split-off flat band that derives from the monolayer Γ states. Using advanced data analysis, we directly quantify the moiré potential from our data. We further demonstrate that the global valence band maximum in $tWSe_2$ is close in energy to this flat band but derives from the monolayer K-states which show weaker superlattice effects. These results constrain theoretical models and open the perspective that Γ-valley flat bands might be involved in the correlated physics of twisted WSe_2.

arXiv:2211.01192v1 [cond-mat.str-el] 2 Nov 2022

The bonding characteristics of van der Waals materials naturally lead to moiré superlattices at interfaces with a lattice mismatch or small twist angle. Exploiting this tuning knob in graphene, WSe_2 and other transition metal dichalcogenides (TMDs) revealed a wealth of non-trivial many-body phases that are not observed in the parent materials. Examples include Mott- and Mott-Wigner like insulating states [1–8], exciton insulators [9, 10], magnetism [9, 11], superconductivity [12, 13] and strange metal phases [5, 14].

The correlated phases in semiconductor moiré systems are generally attributed to strong correlations in monolayer K-states that form flat minibands in the moiré superlattice. However, imaging such mini bands in momentum space proved challenging and key-questions such as the band width, the magnitude of the mini gaps and even from which monolayer valley the mini bands derive remain largely open.

Ab-initio calculations of $tWSe_2$ and other twisted TMDs are thus far limited to isolated bilayers without substrate or encapsulation and do not include doping or displacement fields [15–20]. Moreover, they disagree over the strength of superlattice effects and the nature of the mini-bands at the top of the valence band. Most natural 2H TMD bilayers have the valence band maximum (VBM) at the Γ-point where states derive from the antibonding metal d_{z^2} / chalcogen p_z orbital. However, in 2H WSe_2 (and $MoTe_2$) the large spin-orbit splitting of the metal d_{xy} / $d_{x^2-y^2}$ derived states at K shifts the global VBM to the K-point [21, 22]. Recent large scale density functional calculations find that twist angles below $\approx 3°$ tip this balance and move the VBM of $tWSe_2$ back to Γ [17]. A VBM at Γ was also reported in an ARPES study of twisted double bilayer WSe_2 [23]. Other calculations for different twist angles [16, 19, 20] and a recent experiment at $5.1°$ twist angle [24], find that the VBM derives from monolayer K states.

The nature of the VBM states is crucial because the effective low-energy models used to study correlation effects in twisted TMDs differ for Γ and K states. For Γ derived states, theoretical studies find an emergent honeycomb symmetry with a moiré mini-band structure that resembles artificial graphene [16, 17, 19, 20]. For K-derived states, on the other hand, recent theoretical work found a parabolic moiré VBM at K on the mini-Brillouin zone [17] and an electric field induced topological insulator phase [25]. These differences have obvious implications for the interpretation of transport measurements that are currently being performed and that exhibit a plethora of exciting new phenomena.

The strength of superlattice effects is commonly parameterized by an effective moiré potential. However, estimates of the moiré potential in the literature show a considerable spread ranging from a few milli electron volt (meV) up to hundreds of meV [16, 18, 26, 27]. Previous μ-ARPES studies on $tWSe_2$ and other TMD moiré systems found signatures of replica bands shifted by the moiré reciprocal lattice vector but could not resolve flat moiré mini bands or estimate the effective moiré potential [24, 28, 29]. Scanning tunneling microscopy (STM) studies of $tWSe_2$ found that the local density of states is spatially modulated and, depending on energy and twist-angle, can have triangular, honeycomb or Kagome symmetry [24, 30, 31]. STM further revealed a rich structure of tunneling spectra in the valence band consistent with the formation of moiré minibands. Correlating the real space information from STM with band structure calculations is, however, non-trivial.

Here, we report the direct observation of a flat moiré mini band in $tWSe_2$. The flat band derives from the monolayer Γ-states and is in close proximity to the global VBM opening the possibility that the Γ-valley flat band participates in the correlated phases of $tWSe_2$. We estimate the band width of the moiré mini-band and determine the moiré potential from a

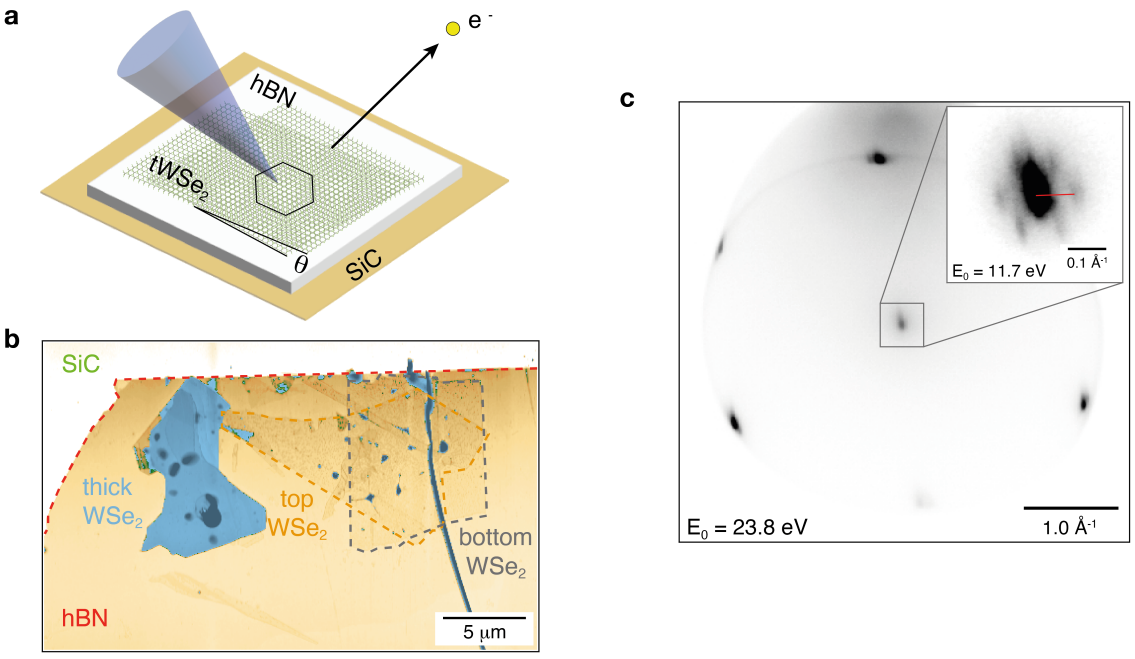


FIG. 1. **Device layout and characterization** (a) Schematic of the μ-ARPES experiment on $tWSe_2$. Heterostructures of $tWSe_2$ on hBN were produced with a tear and stack method and studied with synchrotron based micro-focus ARPES (for details, see Methods). The black hexagon indicates the moiré unit cell for an arbitrary twist angle θ. (b) Topographic atomic force microscopy image of the van der Waals heterostructure. The scale bar is 5 μm. (c) μ-LEED pattern of the twisted bilayer WSe_2. The inset shows a zoom of the (0,0) spot with the satellite peaks used to quantify the moiré wavelength. The red line indicates a reciprocal moiré superlattice vector.

quantitative analysis of the ARPES data.

Fig. 1 illustrates the methodology used in our study. We fabricate the $tWSe_2$ structure with the tear and stack method using a polypropylene carbonate (PPC) stamp, first picking up an hBN flake and then the WSe_2 layers [32]. Prior to the ARPES measurements, we invert the stack, release it on a graphitized SiC substrate and sublimate the PPC in vacuum. This technique avoids any contact of $tWSe_2$ with polymers, which facilitates obtaining a clean, polymer-free sample surface. We determine the precise twist angle of the heterostructure used for the μ-ARPES experiments from micro-focus low-energy electron diffraction (μLEED) (see Fig. 1). We first use the three-fold symmetry of the μLEED patterns in TMDs [33] to independently confirm the stacking angle near $\approx 60°$, corresponding to a 2H structure. A zoom-in around the $(0,0)$ specular beam reveals six satellite spots that define a moiré mini Brillouin zone (BZ) with a reciprocal lattice vector $G^{\text{Moiré}} \approx 1\ \text{nm}^{-1}$ corresponding to a moiré wavelength of $a_M = 7.3$ nm and a twist angle $\theta = 57.4 \pm 0.1°$. Note that the moiré mini-BZ is rotated by $90°$ with respect to the atomic BZ defined by the main diffraction spots. Measurements at multiple locations on the $tWSe_2$ indicate a twist angle variation of no more than $0.4°$ in the sample studied here.

Figure 2 shows the valence band dispersion of $tWSe_2$ over the entire monolayer Brillouin zone. At first glance, the overall dispersion is reminiscent of a natural 2H bilayer with parabolic band maxima at Γ and K [21]. However, a closer inspection of the data near Γ (Fig. 2d) reveals the presence of additional features on a much smaller energy scale that are absent in untwisted 2H WSe_2. Extracting energy distribution curves (EDC) at Γ from the data in Fig. 2d, we resolve three distinct components in $tWSe_2$ (features *A, B, C* in Fig. 2b), in stark contrast to the EDC of 2H WSe_2, which shows a single peak only. This splitting into multiple peaks in $tWSe_2$ is a fingerprint of moiré mini bands. It also shows that moiré superlattice effects alter valley energies. None of the 3 components in $tWSe_2$ can be trivially associated with the single peak in 2H WSe_2. This suggests that moiré effects can shift valleys by several ten meV, which is non-negligible in bilayer WSe_2 because of the close proximity in energy of states at Γ and K [21, 22, 34].

The spectrum at K shows a well defined onset but no clear multi-peak structure. This implies weaker superlattice effects than at Γ, in qualitative agreement with theoretical predictions [16, 17]. We quantify valley energies from experiment by comparing the highest-energy feature A in the multi-peak fit at Γ with a fit of the onset of spectral weight at K. This shows that the Γ-valley in $tWSe_2$ lies 90 ± 20 meV lower than the global VBM measured at K. This is comparable to the variation of valley energies with strain [35], doping and displacement fields [36] and only slightly larger than the chemical potential of WSe_2 at relevant densities, all suggesting the

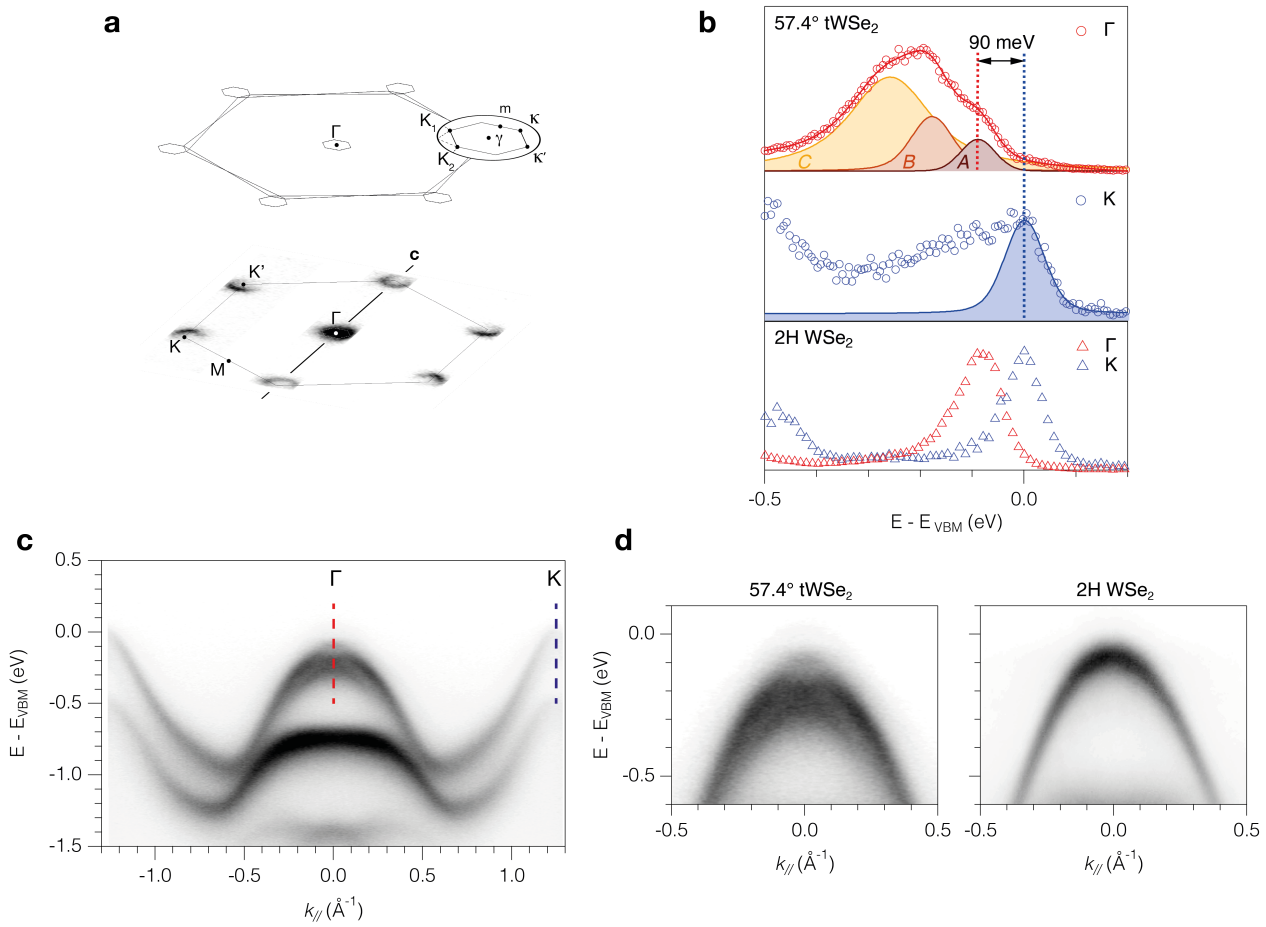


FIG. 2. **Valence band maximum in $tWSe_2$.** (a) ARPES constant energy map 200 meV below the VBM. The Brillouin zones (BZs) of the two twisted monolayers are indicated by grey hexagons. Small hexagons show the moiré mini BZs. (b) Energy distribution curves (EDCs) from $tWSe_2$ and untwisted 2H WSe_2 extracted at Γ and K of the monolayer BZ. The EDCs from $tWSe_2$ are fit with three and one Lorentzians, respectively, convolved with a Gaussian of 70 meV full width half maximum to account for energy resolution and inhomogeneous broadening. (c) ARPES band dispersion of $tWSe_2$ measured along ΓK over the large monolayer BZ. (d) Zoom-in of the ARPES spectral functions of twisted and untwisted WSe_2 near the Γ point.

Γ-valley flat band might contribute to the correlated phases observed in $tWSe_2$ [4, 5, 9].

Fig. 3a shows the complex spectral function of the moiré states along both high symmetry directions. Near the Γ point we can directly trace the dispersion of features *A, B, C* from curve fits of the EDCs shown in Fig. 3c. Additional, more dispersive features at higher energy are evident in the raw image and curvature plots of the ARPES data. The topmost feature A defines the first moiré miniband. Consistent with the curvature plots, our fits show that this band is nearly dispersionless and separated by a gap of several 10 meV from other states. Tracing feature A over the full mini BZ, we estimate a band width of the first moiré mini band of ≈ 10 meV. This is small compared to the Hubbard interaction estimated as $U \approx e^2/(4\pi\epsilon\epsilon_0 d) \approx 80$ meV (assuming $\epsilon \approx 5$ and $d \approx a_M/2 = 3.6$ nm) placing half-filled 57.4° $tWSe_2$ in the strongly correlated regime.

We now compare our data to a generic effective continuum model describing the motion of electrons in the bonding and antibonding valence band of twisted TMDs in the presence of an effective moiré potential [18]:

$$H = \begin{bmatrix} -\frac{\hbar^2\mathbf{k}^2}{2m^\star} + V_1 & t_\perp(\mathbf{k}) \\ t_\perp(\mathbf{k}) & \frac{\hbar^2\mathbf{k}^2}{2m^\star} + V_2 \end{bmatrix}$$

$$V_{1,2} = 2V_0 \sum_{j=1}^{3} \cos(\mathbf{G}_j^{\text{Moiré}} \cdot \mathbf{r} \pm \phi) \qquad (1)$$

Here, the effective mass m^* and interlayer hopping $t_\perp(\mathbf{k})$ parametrize the band structure of untwisted bilayers. We determine both of these parameters from fits to density functional theory calculations. Supplementary Fig. 5 shows that this is in excellent agreement with ARPES data from exfoliated 2H WSe_2. The moiré physics is described with the effective potential $V_{1,2}$, which we expand in a first order Fourier series in the moiré wave vectors $\mathbf{G}_j^{\text{Moiré}}$ with phase factors ϕ

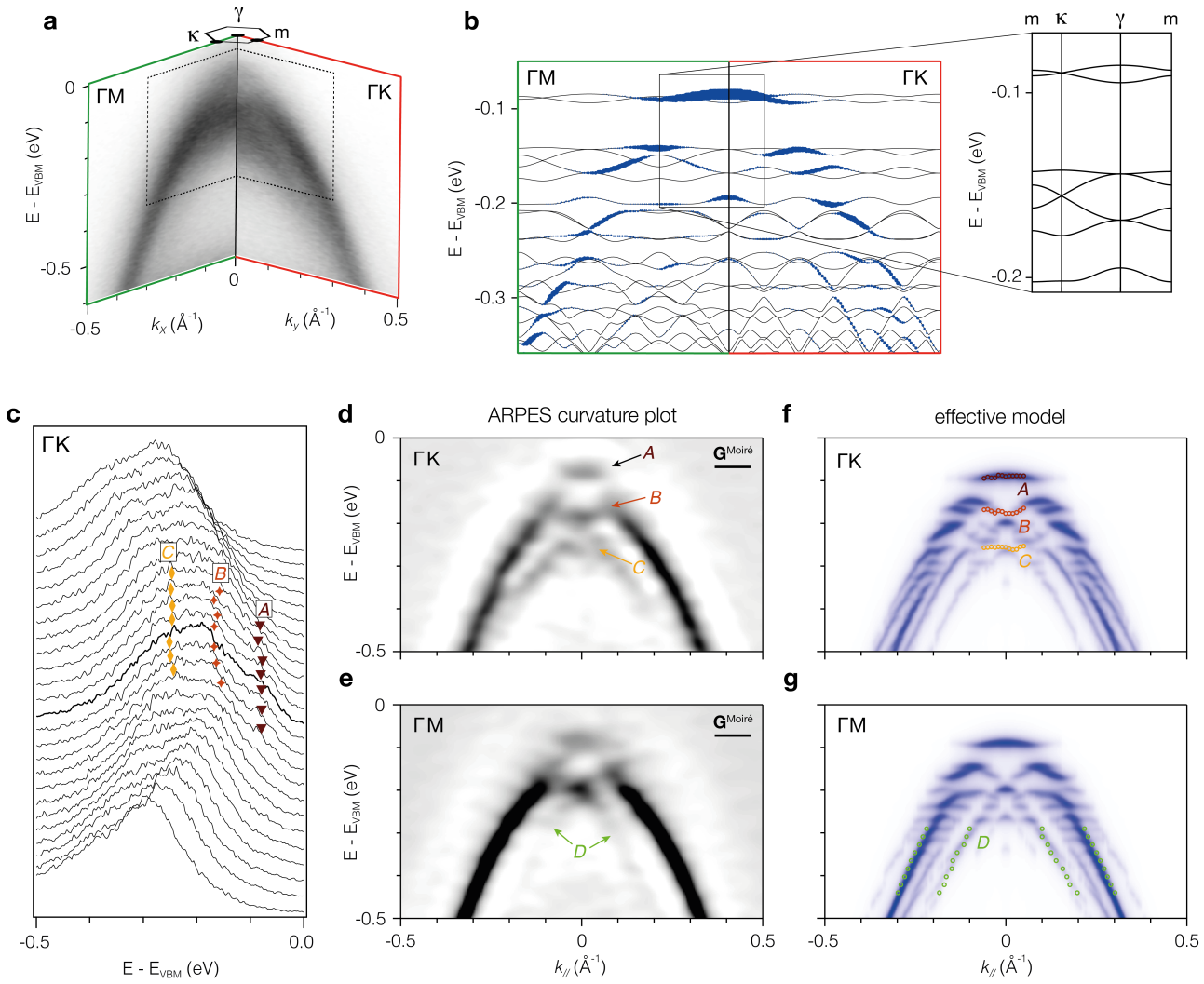


FIG. 3. **Moiré mini bands.** (a) ARPES band dispersions near the Γ point along the two high symmetry directions. The small hexagon indicates the mini BZ. (b) Band dispersion (black) and spectral weights (blue) of the effective Hamiltonian in Eq. 1 with parameters $V_0 = 48$ meV and $\phi = 121°$. (c) Stack of EDCs in a momentum window of 0.2 Å^{-1} along K-Γ-K'. Markers indicate the position of the three Lorentzian peaks obtained from curve fits. (d,e) Curvature plots of the ARPES band dispersions along the K-Γ-K' and M-Γ-M directions, respectively. The scale bar corresponds to a moiré reciprocal lattice vector. (f,g) Simulated spectral function of the effective Hamiltonian with the same parameters used in (c). For a visual comparison with the curvature plots in (d,e) we use a Lorentzian broadening of 10 meV which is smaller than the optimal value found in the numerical optimization (see supplementary information, section II).

that change sign with layer to be consistent with the 2-fold rotational symmetry with layer exchange.

This model reproduces the band structure found in previous theoretical work [16, 18] with the characteristic Dirac cones at κ in the first moiré mini-band for a wide range of phases ϕ (Fig. 3b).

For a direct comparison with the ARPES data, we first calculate spectral weights by projecting the eigenstates of H on plane wave states with momentum $\mathbf{k}$ (Fig. 3b,f,g) [37–39]. Performing calculations for different combinations of V_0, ϕ we identify three principal features that are sensitive to the model parameters: *i)* As expected from theory, the gap between the first two moiré subbands is controlled by V_0; *ii)* the spectral weight distribution of the dispersive features at high binding energy is very sensitive to the phase ϕ, while *iii)* the separation of features A, B, C is determined by a combination of V_0 and ϕ. Hence, V_0 and ϕ are sufficiently independent to be determined from our data. To do so in an unbiased way we calculate $\approx 5'000$ spectral functions for different parameters and determine the least square difference to the raw data. This yields $V_0 = 48 \pm 8$ meV and $\phi = 121° \pm 7°$ where the error bars are estimated from the standard deviation of the parameters of all calculations weighted by the inverse of their square difference to the data.

Fig. 3f,g shows the continuum model spectral functions with the above determined parameters and a reduced broad-

ening, demonstrating a good overall agreement with the data. This confirms the interpretation of the main spectral features in terms of moiré mini-bands. The calculations clearly reproduce a split-off flat band that is highly localized in momentum space (feature A) suggesting a wave function extending over much of the moiré unit cell. The band width (Γ to M dispersion) of the first subband in our model is 6 meV, in fair agreement with our experimental estimate of 10 meV. The calculations also reproduce the weakly dispersive features B, C as well as the side band D. We note that the latter has been reported previously in Ref. [24] where its separation from the main band was identified with the moiré reciprocal lattice vector. Our calculations show that such an interpretation is not evident as a multitude of dispersive side bands are expected at various momenta.

The phase $\phi \approx 120^\circ$ determined from our numerical analysis confirms the emergent honeycomb symmetry of the first subband, predicted by large scale density functional theory calculations [16–18]. We note that a honeycomb charge distribution was also reported in some STM spectroscopic imaging experiments [24, 30] while another recent STM study found a triangular symmetry for the highest visible subband [31].

Our quantification of superlattice effects in $tWSe_2$ provides a benchmark for large scale DFT calculations. More broadly, our work lends strong support to an interpretation of the remarkable transport and optical properties of $tWSe_2$ in terms of a correlated flat band system. However, our work also shows that $tWSe_2$ lacks the clear separation of energy scales needed for a description by a single band Hubbard model. The moiré potential of $V_0 = 48$ meV determined from our quantitative analysis is comparable to the energy difference of Γ and K-valleys and also to shifts in valley energies predicted under realistic doping, displacement field and strain values [35, 36]. Moreover, for the twist angle studied here, the onsite interaction U likely exceeds the moiré potential and thus the gap between subband manifolds. Accounting for this complexity will be essential for the interpretation of magneto-transport and optical measurements and will require the development of multi-band theoretical models.

ACKNOWLEDGMENTS

This work was supported by the Swiss National Science Foundation (SNSF) under grants 184998, 178891. LR acknowledges support from a SNSF Ambizione fellowship 174208. TAdJ acknowledges financial support by the Netherlands Organisation for Scientific Research (NWO/OCW) as part of the Frontiers of Nanoscience (NanoFront) program. We acknowledge Diamond Light Source for time on Beamline I05 under Proposal SI29021.

METHODS

Commercially available hexagonal Boron Nitride (hBN) and WSe_2 have been exfoliated in air on 285 nm SiO_2/Si wafers. Crystal flakes with a specific thickness were recognized from their optical contrast under a microscope, and the thickness was later confirmed by AFM measurements. Heterostructures were assembled in a glove box using a motorized transfer system. Transfer stamps were fabricated by placing a spin-coated PPC film on a dome-shaped handle made of polydimethylsiloxane (PDMS). To fabricate the heterostructure used in this work, we first picked up a large 17 nm thick hexagonal boron nitride (hBN) flake, whose sharp and straight edge was later employed to tear a monolayer WSe_2 flake in two parts while simultaneously picking up one of them. Subsequently, the stage was rotated by 57° and the remaining WSe_2 monolayer was picked up. Finally, the PPC film was detached from the PDMS base, flipped and released on a graphetized SiC substrate. Polymer residues and other contaminants were removed by annealing in ultra-high vacuum at 400°C for 2 hours.

Photoemission experiments were performed at the nanoARPES endstation of the I05 beamline at Diamond Light Source, Didcot (UK) and the Antares beamline of Soleil synchrotron, France. The data shown in this manuscript were acquired at Diamond I05 using 80 eV light focused to $\approx 1 \times 1$ μm^2 spot size using a Fresnel zone plate. Immediately prior to the experiments, the sample was annealed in ultra-high vacuum at 400°C for 30 minutes before transferring it *in-situ* to the experimental chamber. The photoemission experiments were performed at 180 K using an energy and momentum resolution of ≈ 20 meV and ≈ 0.01 Å^{-1}. Note that the $tWSe_2$ was not in direct electrical contact with the chamber ground. Nevertheless, charging effects remained well below the resolution of this experiment, which we attribute to the high photo-conductivity of hBN.

Low-Energy Electron Microscopy (LEEM) and μLEED were performed after photoemission experiments in the SPECS P90 based ESCHER system at Leiden University. Before measurements, the sample was reheated to 350°C (as measured by a pyrometer with emissivity set to 1.0) in the ultrahigh-vacuum of the measurement chamber (base pressure $< 1.0 \times 10^{-9}$mbar). The sample was located on the substrate using photo-emission electron microscopy with an unfiltered mercury short-arc lamp. Initial μLEED measurements confirming the 2H-like geometry where performed using a 1.1 μm effective diameter circular illumination aperture. Subsequently the satellite diffraction spots arising from the moiré lattice were measured using a 0.23 μm effective diameter illumination aperture. Twist angle variation was determined by scanning the sample stage over the area used for μ-ARPES experiments while recording diffraction patterns using the same illumination aperture.

* These authors contributed equally to this work.

[1] E. C. Regan, D. Wang, C. Jin, M. I. Bakti Utama, B. Gao, X. Wei, S. Zhao, W. Zhao, Z. Zhang, K. Yumigeta, M. Blei, J. D. Carlström, K. Watanabe, T. Taniguchi, S. Tongay, M. Crommie, A. Zettl, and F. Wang, Mott and generalized Wigner crystal states in WSe_2/WS_2 moiré superlattices, Nature **579**, 359 (2020).

[2] Y. Tang, L. Li, T. Li, Y. Xu, S. Liu, K. Barmak, K. Watanabe, T. Taniguchi, A. H. MacDonald, J. Shan, and K. F. Mak, Simulation of Hubbard model physics in WSe_2/WS_2 moiré superlattices, Nature **579**, 353 (2020).

[3] Y. Xu, S. Liu, D. A. Rhodes, K. Watanabe, T. Taniguchi, J. Hone, V. Elser, K. F. Mak, and J. Shan, Correlated insulating states at fractional fillings of moirésuperlattices, Nature **587**, 214 (2020).

[4] L. Wang, E.-M. Shih, A. Ghiotto, L. Xian, D. A. Rhodes, C. Tan, M. Claassen, D. M. Kennes, Y. Bai, B. Kim, K. Watanabe, T. Taniguchi, X. Zhu, J. Hone, A. Rubio, A. N. Pasupathy, and C. R. Dean, Correlated electronic phases in twisted bilayer transition metal dichalcogenides, Nature Materials **19**, 861 (2020).

[5] A. Ghiotto, E.-M. Shih, G. S. S. G. Pereira, D. A. Rhodes, B. Kim, J. Zang, A. J. Millis, K. Watanabe, T. Taniguchi, J. C. Hone, L. Wang, C. R. Dean, and A. N. Pasupathy, Quantum criticality in twisted transition metal dichalcogenides, Nature **597**, 345 (2021).

[6] T. Li, S. Jiang, L. Li, Y. Zhang, K. Kang, J. Zhu, K. Watanabe, T. Taniguchi, D. Chowdhury, L. Fu, J. Shan, and K. F. Mak, Continuous mott transition in semiconductor moiré superlattices, Nature **597**, 350 (2021).

[7] Y. Shimazaki, I. Schwartz, K. Watanabe, T. Taniguchi, M. Kroner, and A. Imamoğlu, Strongly correlated electrons and hybrid excitons in a moiréheterostructure, Nature **580**, 472 (2020).

[8] H. Li, S. Li, E. C. Regan, D. Wang, W. Zhao, S. Kahn, K. Yumigeta, M. Blei, T. Taniguchi, K. Watanabe, S. Tongay, A. Zettl, M. F. Crommie, and F. Wang, Imaging two-dimensional generalized wigner crystals, Nature **597**, 650 (2021).

[9] Y. Xu, K. Kang, K. Watanabe, T. Taniguchi, K. F. Mak, and J. Shan, A tunable bilayer Hubbard model in twisted WSe_2, Nature Nanotechnology 10.1038/s41565-022-01180-7 (2022).

[10] Z. Zhang, E. C. Regan, D. Wang, W. Zhao, S. Wang, M. Sayyad, K. Yumigeta, K. Watanabe, T. Taniguchi, S. Tongay, M. Crommie, A. Zettl, M. P. Zaletel, and F. Wang, Correlated interlayer exciton insulator in heterostructures of monolayer WSe_2 and moiré WS_2/WSe_2, Nature Physics 10.1038/s41567-022-01702-z (2022).

[11] A. L. Sharpe, E. J. Fox, A. W. Barnard, J. Finney, K. Watanabe, T. Taniguchi, M. A. Kastner, and D. Goldhaber-Gordon, Emergent ferromagnetism near three-quarters filling in twisted bilayer graphene, Science **365**, 605 (2019).

[12] Y. Cao, V. Fatemi, S. Fang, K. Watanabe, T. Taniguchi, E. Kaxiras, and P. Jarillo-Herrero, Unconventional superconductivity in magic-angle graphene superlattices, Nature **556**, 43 (2018).

[13] X. Lu, P. Stepanov, W. Yang, M. Xie, M. A. Aamir, I. Das, C. Urgell, K. Watanabe, T. Taniguchi, G. Zhang, A. Bachtold, A. H. MacDonald, and D. K. Efetov, Superconductors, orbital magnets and correlated states in magic-angle bilayer graphene, Nature **574**, 653 (2019).

[14] A. Jaoui, I. Das, G. Di Battista, J. Díez-Mérida, X. Lu, K. Watanabe, T. Taniguchi, H. Ishizuka, L. Levitov, and D. K. Efetov, Quantum critical behaviour in magic-angle twisted bilayer graphene, Nature Physics **18**, 633 (2022).

[15] M. H. Naik and M. Jain, Ultraflatbands and shear solitons in moiré patterns of twisted bilayer transition metal dichalcogenides, Phys. Rev. Lett. **121**, 266401 (2018).

[16] M. Angeli and A. H. MacDonald, Gamma valley transition metal dichalcogenide moire bands, Proceedings of the National Academy of Sciences **118**, e2021826118 (2021).

[17] V. Vitale, K. Atalar, A. A. Mostofi, and J. Lischner, Flat band properties of twisted transition metal dichalcogenide homo- and heterobilayers of MoS_2, $MoSe_2$, WS_2 and WSe_2, 2D Materials **8** (2021).

[18] Y. Zhang, T. Liu, and L. Fu, Electronic structures, charge transfer, and charge order in twisted transition metal dichalcogenide bilayers, Phys. Rev. B **103**, 155142 (2021).

[19] T. Devakul, V. Crépel, Y. Zhang, and L. Fu, Magic in twisted transition metal dichalcogenide bilayers, Nature Communications **12**, 6730 (2021).

[20] S. Kundu, M. H. Naik, H. R. Krishnamurthy, and M. Jain, Moiré induced topology and flat bands in twisted bilayer WSe_2: A first-principles study, Physical Review B **105**, L081108 (2022).

[21] N. R. Wilson, P. V. Nguyen, K. Seyler, P. Rivera, A. J. Marsden, Z. P. L. Laker, G. C. Constantinescu, V. Kandyba, A. Barinov, N. D. M. Hine, X. Xu, and D. H. Cobden, Determination of band offsets, hybridization, and exciton binding in 2D semiconductor heterostructures, Science Advances **3**, e1601832 (2017).

[22] J. Lindlau, M. Selig, A. Neumann, L. Colombier, J. Förste, V. Funk, M. Förg, J. Kim, G. Berghäuser, T. Taniguchi, K. Watanabe, F. Wang, E. Malic, and A. Högele, The role of momentum-dark excitons in the elementary optical response of bilayer WSe_2, Nature Communications **9**, 10.1038/s41467-018-04877-3 (2018).

[23] L. An, X. Cai, D. Pei, M. Huang, Z. Wu, Z. Zhou, J. Lin, Z. Ying, Z. Ye, X. Feng, R. Gao, C. Cacho, M. Watson, Y. Chen, and N. Wang, Interaction effects and superconductivity signatures in twisted double-bilayer WSe_2, Nanoscale Horiz. **5**, 1309 (2020).

[24] D. Pei *et al.*, Observation of Γ-valley moiré bands and emergent hexagonal lattice in twisted transition metal dichalcogenides, arXiv:2205.13788 (2022).

[25] F. Wu, T. Lovorn, E. Tutuc, I. Martin, and A. H. MacDonald, Topological insulators in twisted transition metal dichalcogenide homobilayers, Phys. Rev. Lett. **122**, 086402 (2019).

[26] S. Shabani, D. Halbertal, W. Wu, M. Chen, S. Liu, J. Hone, W. Yao, D. N. Basov, X. Zhu, and A. N. Pasupathy, Deep moirépotentials in twisted transition metal dichalcogenide bilayers, Nature Physics **17**, 720 (2021).

[27] W. T. Geng, V. Wang, Y. C. Liu, T. Ohno, and J. Nara, Moiré Potential, Lattice Corrugation, and Band Gap Spatial Variation in a Twist-Free $MoTe_2/MoS_2$ Heterobilayer, The Journal of Physical Chemistry Letters **11**, 2637 (2020), pMID: 32188242.

[28] S. Ulstrup, R. J. Koch, S. Singh, K. M. McCreary, B. T. Jonker, J. T. Robinson, C. Jozwiak, E. Rotenberg, A. Bostwick, J. Katoch, and J. A. Miwa, Direct observation of minibands in a twisted graphene/WS_2 bilayer, Science Advances **6**, eaay6104 (2020).

[29] S. Xie, B. D. Faeth, Y. Tang, L. Li, C. T. Parzyck, D. Chowdhury, Y.-H. Zhang, C. Jozwiak, A. Bostwick, E. Rotenberg, J. Shan, K. F. Mak, and K. M. Shen, Direct observation of distinct minibands in moiré superlattices (2020).

[30] Z. Zhang, Y. Wang, K. Watanabe, T. Taniguchi, K. Ueno, E. Tutuc, and B. J. LeRoy, Flat bands in twisted bilayer transition metal dichalcogenides, Nature Physics **16**, 1093 (2020).

[31] E. Li, J.-X. Hu, X. Feng, Z. Zhou, L. An, K. T. Law, N. Wang, and N. Lin, Lattice reconstruction induced multiple ultra-flat

bands in twisted bilayer WSe_2, Nature Communications **12**, 5601 (2021).

[32] K. Kim, M. Yankowitz, B. Fallahazad, S. Kang, H. C. P. Movva, S. Huang, S. Larentis, C. M. Corbet, T. Taniguchi, K. Watanabe, S. K. Banerjee, B. J. LeRoy, and E. Tutuc, van der waals heterostructures with high accuracy rotational alignment, Nano Letters **16**, 1989 (2016).

[33] T. A. de Jong, J. Jobst, H. Yoo, E. E. Krasovskii, P. Kim, and S. J. van der Molen, Measuring the local twist angle and layer arrangement in Van der Waals heterostructures, physica status solidi (b) **255**, 1800191 (2018).

[34] P. V. Nguyen, N. C. Teutsch, N. P. Wilson, J. Kahn, X. Xia, A. J. Graham, V. Kandyba, A. Giampietri, A. Barinov, G. C. Constantinescu, N. Yeung, N. D. M. Hine, X. Xu, D. H. Cobden, and N. R. Wilson, Visualizing electrostatic gating effects in two-dimensional heterostructures, Nature **572**, 220 (2019).

[35] B. Amin, T. P. Kaloni, and U. Schwingenschlögl, Strain engineering of WS_2, WSe_2, and WTe_2, RSC Adv. **4**, 34561 (2014).

[36] T. Brumme, M. Calandra, and F. Mauri, First-principles theory of field-effect doping in transition-metal dichalcogenides: Structural properties, electronic structure, Hall coefficient, and electrical conductivity, Phys. Rev. B **91**, 155436 (2015).

[37] J. Voit, L. Perfetti, F. Zwick, H. Berger, G. Margaritondo, G. Grüner, H. Höchst, and M. Grioni, Electronic structure of solids with competing periodic potentials., Science **290**, 501 (2000).

[38] S. Moser, An experimentalist's guide to the matrix element in angle resolved photoemission, Journal of Electron Spectroscopy and Related Phenomena **214**, 29 (2017).

[39] S. Lisi, X. Lu, T. Benschop, T. A. de Jong, P. Stepanov, J. R. Duran, F. Margot, I. Cucchi, E. Cappelli, A. Hunter, A. Tamai, V. Kandyba, A. Giampietri, A. Barinov, J. Jobst, V. Stalman, M. Leeuwenhoek, K. Watanabe, T. Taniguchi, L. Rademaker, S. J. van der Molen, M. P. Allan, D. K. Efetov, and F. Baumberger, Observation of flat bands in twisted bilayer graphene, Nature Physics **17**, 189 (2021).